Temperature-Modulated Selective Detection of Part-per-Trillion NO_2 Using Platinum Nanocluster Sensitized 3D Metal Oxide Nanotube Arrays

*Zhilong Song, Wenying Tang, Zhesi Chen, Zhu'an Wan, Chak Lam Jonathan Chan, Chen Wang, Wenhao Ye, and Zhiyong Fan**

Semiconductor chemiresistive gas sensors play critical roles in a smart and sustainable city where a safe and healthy environment is the foundation. However, the poor limits of detection and selectivity are the two bottleneck issues limiting their broad applications. Herein, a unique sensor design with a 3D tin oxide (SnO_2) nanotube array as the sensing layer and platinum (Pt) nanocluster decoration as the catalytic layer, is demonstrated. The Pt/SnO_2 sensor significantly enhances the sensitivity and selectivity of NO_2 detection by strengthening the adsorption energy and lowering the activation energy toward NO_2. It not only leads to ultrahigh sensitivity to NO_2 with a record limit of detection of 107 parts per trillion, but also enables selective NO_2 sensing while suppressing the responses to interfering gases. Furthermore, a wireless sensor system integrated with sensors, a microcontroller, and a Bluetooth unit is developed for the practical indoor and on-road NO_2 detection applications. The rational design of the sensors and their successful demonstration pave the way for future real-time gas monitoring in smart home and smart city applications.

1. Introduction

Chemical-sensing devices take significant roles in our daily life for real-time monitoring the air quality, health conditions, and industrial and agricultural production processes.[1–4] In particular, the detection of nitrogen dioxide (NO_2), a toxic and corrosive gas primarily emitted from the burning fossil fuels, is of significant importance.[5,6] NO_2 will cause the negative effect on respiratory system of human beings, having a great risk on children and the elderly, especially population affected by corona virus disease (COVID-19).[7] The United States Environmental Protection Agency (US EPA) has set safety levels for environmental exposure to NO_2 at 100 ppb h^{-1}, and 53 ppb over one year. In addition, NO_2 can also be recognized as an important endogenous gas (parts per billion [ppb]/parts per trillion [ppt] level) for potential disease diagnoses (e.g., asthma and inflammatory bowel identification).[8–11] However, NO_2 always exists under the presence of other interfering gases, such as formaldehyde (FA), toluene, acetone, and SO_2, and the sensitive and selective detection trace amount of NO_2 among the interfering gases remains a bottleneck challenge.

Chemiresistive gas sensors made of metal-oxide semiconductors, such as tin oxide (SnO_2)[12–14] and zinc oxide (ZnO),[15–18] possess a number of highly attractive merits, including small formfactor and being integratable with other semiconductor devices, long life-time, and low cost. Thus, they are playing the critical roles in a smart and sustainable city for safety and healthy monitoring.[19–23] However, the poor limit of detection (LOD) and selectivity are the two main bottlenecks limiting their wide application.[24,25] Well-established methods were utilized to improve the gas-sensing performance,[26,27] and earlier works have demonstrated that LOD of chemiresistive gas sensors can be improved by employing low-dimensional and nanostructured materials with high surface-to-volume ratio.[28–32] Meanwhile, a more challenging issue is poor selectivity, namely, the interaction between the oxide surface and gas molecules often leads to similar or comparable response signals.[33–36] In order to improve the selectivity, it is required that the gas sensors to be highly reactive toward the target gas but with negligible response to the interfering gases.[37] Sorption-filter column implantation in front of sensors is a classic method dominating in gas chromatography sensor systems, it could improve the selectivity by blocking the interfering gases to the sensor films, but surfers from the issues of adsorption saturation that requires replacement or regeneration of the

---

Z. Song, W. Tang, Z. Chen, Z. Wan, C. L. J. Chan, C. Wang, W. Ye, Z. Fan
Department of Electronic and Computer Engineering
Energy Institute
The Hong Kong University of Science and Technology
Clear Water Bay, Kowloon, Hong Kong SAR 999077, China
E-mail: eezfan@ust.hk

Z. Song, W. Tang, Z. Chen, Z. Wan, C. L. J. Chan, C. Wang, W. Ye, Z. Fan
The Hong Kong University of Science and Technology-Shenzhen
Research Institute
Shenzhen 518057, China

Z. Song
Institute for Energy Research
Key Laboratory of Zhenjiang
Jiangsu University
Zhenjiang, Jiangsu 212013, China

The ORCID identification number(s) for the author(s) of this article can be found under https://doi.org/10.1002/smll.202203212.

DOI: 10.1002/smll.202203212

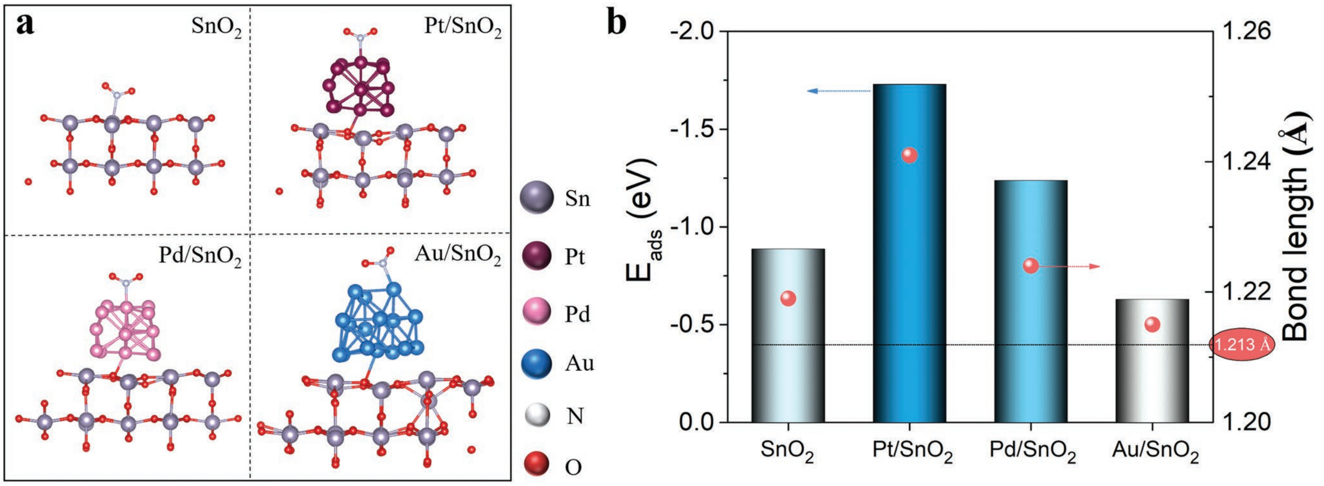

Figure 1. DFT calculations. a) Optimized structures (side view) of SnO$_2$ and noble metal (Pt, Pd, and Au) decorated SnO$_2$ for NO$_2$ adsorption. b) Adsorption energies (E_{ads}) for NO$_2$ adsorption on SnO$_2$ and noble metal (Pt, Pd, and Au) decorated SnO$_2$ and their corresponding N—O bond length (N—O bond length in free NO$_2$ is 1.213 Å).

column, leading to the prolonged sensor response and recovery times.[38,39] Catalytic-assistant method by coating noble metal onto sensing materials is considered as promising approach to solve the selectivity issue. The noble metal on the surface would strengthen an electrical and chemical integration with the target gas by lowering down activation energy (E_a), promoting a specific surface reaction with enhanced selectivity.[40,41] However, the strategies that could simultaneously solve the LOD and selectivity issues remain challenging and still need improvement.

In the present study, we report a sensor design using 3D SnO$_2$ nanotube array as the sensing layer and platinum (Pt) nanocluster decoration as the catalytic layer, realized by two-step atomic layer deposition (ALD) method. The Pt nanoclusters can not only increase the adsorption energy (E_{ads}) toward the target gas of NO$_2$ compared with the pure SnO$_2$, but also lower down the activation energy (E_a), speeding up the surface reaction. This significantly enhances the sensitive and selective NO$_2$ detection. The as-fabricated Pt/SnO$_2$ sensor achieves an ultrahigh sensitivity to NO$_2$ with the record LOD down to 107 ppt through the operation temperature modulation, and it simultaneously enables the selective NO$_2$ sensing while suppressing the responses to interfering gases (e.g., SO$_2$, FA, acetone, and toluene) at the optimized operation temperature (≈200 °C). Furthermore, we construct a portable sensor system integrated with sensors, microcontroller (MCU) and Bluetooth unit for practical indoor and on-road NO$_2$ detection applications. The rational design of the sensors and their successful demonstration pave the way for the future real-time environmental safety and air quality monitoring in smart home and smart city applications.

2. Results and Discussion

2.1. Design of Potential Pt/SnO$_2$ Sensors

First of all, density functional theory (DFT) calculations are employed to identify the most promising candidate for selective NO$_2$ sensing. The work is guided by the idea that noble metal catalysts could realize the selectivity by accelerating a specific reaction toward the target gas while suppressing the other interfering gases.[42,43] Platinum (Pt), palladium (Pd), and gold (Au) are chosen for SnO$_2$ decoration, and the optimized molecular structures (side view) for NO$_2$ adsorption are shown in **Figure 1**a. The activity and selectivity of the sensors are evaluated by calculating the adsorption energy and N—O bond length of NO$_2$ adsorbed on the surface of the catalysts. The detailed setting of the DFT calculation can be found in Supporting Information (DFT Methods). As displayed in Figure 1b, the Pt/SnO$_2$ structure shows the highest adsorption energy (–1.729 eV) for NO$_2$ molecular adsorption, among the structures of SnO$_2$ (–0.887 eV), Pd/SnO$_2$ (–1.238 eV), and Au/SnO$_2$ (–0.629 eV). And the Pt/SnO$_2$ also induces the largest N—O bond length change ($\Delta\lambda$ = 0.028 Å) than that of SnO$_2$ ($\Delta\lambda$ = 0.006 Å), Pd/SnO$_2$ ($\Delta\lambda$ = 0.011 Å), and Au/SnO$_2$ ($\Delta\lambda$ = 0.002 Å), respectively. The results suggest that Pt/SnO$_2$ structure has a specific interaction energetically favorable for selective adsorption of NO$_2$ molecules. Finally, the Pt/SnO$_2$ structure is identified as the most promising candidate for selective NO$_2$ sensing.

2.2. Pt/SnO$_2$ Sensor Fabrication

The Pt/SnO$_2$ sensors are fabricated by a two-step ALD method[13] employing the 3D nanoporous single-side-opened anodic aluminum oxide (AAO) as the substrate (**Figure 2**a). The 3D nanoporous AAO gives a support for the sensor films deposition, which enables a favorable gas diffusion and provides a large surface area for the gas adsorption. The Pt/SnO$_2$ sensors consist of a thin layer of SnO$_2$ on the AAO wall followed by deposition of a conformal Pt layer. The ALD process generally consists of four sequential steps (1 cycle) for the thin film fabrication (Figure 2b): 1) precursor exposure → 2) purge → 3) reactant exposure → 4) purge. In the detail for SnO$_2$ deposition, the Sn precursor of tetrakis(dimethylamino)tin (Sn(DMA)$_4$) was first introduced

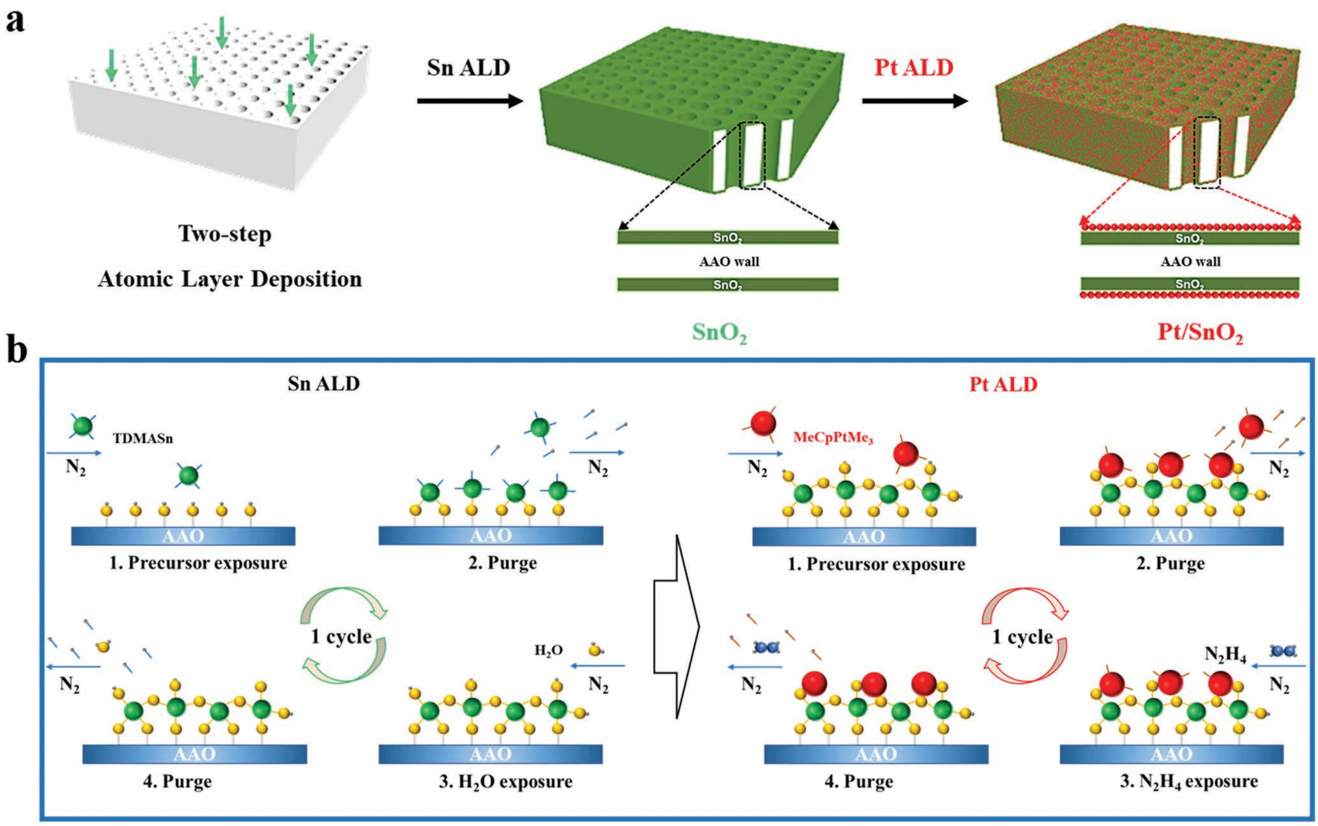

Figure 2. Pt/SnO$_2$ sensor fabrication. a) Schematic diagram of Pt nanoclusters decorated 3D SnO$_2$ nanotube array (Pt/SnO$_2$) fabrication by two-step ALD method. b) The schematic diagram of SnO$_2$ and Pt ALD deposition process.

into the chamber, and pure N$_2$ was used to purge out the unabsorbed precursor when reaching an adsorption equilibrium on the AAO wall (*OH, representing the surface-bound species on AAO wall); then the reactant of H$_2$O was further introduced in to reacted with the adsorbed Sn precursor, resulting in the formation of SnO$_2$ anchoring onto the AAO wall. The surface reaction chemistry can be ascribed as follows.

$$x(*\text{OH})+\text{Sn}(\text{DMA})_4 \rightarrow (*\text{O})_x\,\text{Sn}(\text{DMA})_{4-x}+x\text{HDMA}\uparrow \quad (1)$$

$$(*\text{O})_x\,\text{Sn}(\text{DMA})_{4-x}+\text{H}_2\text{O} \rightarrow x(*\text{OH})+\text{SnO}_2+(4-x)\text{HDMA}\uparrow \quad (2)$$

The over layer of Pt nanoclusters was then deposited onto the SnO$_2$ thin films (*SnO$_2$, representing the active sites on SnO$_2$ surface) to complete the sensing layer fabrication. The Pt ALD process followed the same procedure as SnO$_2$ deposition employing (trimethyl)methylcyclopentadienylplatinum (IV) (MeCpPtMe$_3$) and anhydrous hydrazine (N$_2$H$_4$) as the reaction precursors and surface chemistry can be described as follows.

$$\text{MeCpPtMe}_3+x(*\text{SnO}_2) \rightarrow \text{MeCpPtMe}_{3-x}(*\text{SnO}_2)_x+x\text{CH}_4\uparrow \quad (3)$$

$$\begin{aligned}&\text{MeCpPtMe}_{3-x}(*\text{SnO}_2)_x+\text{N}_2\text{H}_4 \rightarrow\\&\text{Pt}(*\text{SnO}_2)_x+4\text{CH}_4\uparrow+\text{N}_2\uparrow+\text{Cp}\uparrow\end{aligned} \quad (4)$$

The thicknesses of the SnO$_2$ and Pt film in the sensors can be easily controlled by the ALD recipe cycles.

2.3. Pt/SnO$_2$ Sensor Structure Characterization

Figure 3a shows the photograph of 2 cm × 2 cm 3D AAO supporting the Pt decorated SnO$_2$ nanotube array. After the optimization of the SnO$_2$ and Pt thickness by ALD recipe cycles, 3 × 4 sensors on one-chip AAO were obtained with sputtered top patterned Au electrodes and bottom Pt heater electrodes (Figure 3b). The structure diagram of the sensor was clearly displayed in Figure 3c with three components of Au sensor electrodes, sensing material on AAO and Pt heater electrodes. Figure 3d exhibits the SEM image of AAO substrate (50 µm thickness, 500 nm pitch, and 400 nm average pore size) supported the Pt/SnO$_2$ sensing material. In the magnified cross-section view, we can clearly observe the uniform Pt/SnO$_2$ thin films anchoring onto the AAO wall with the average thickness of 12 nm. HRTEM image (Figure 3e) shows the lattice distance of 0.334 nm corresponding to the (110) planes of rutile SnO$_2$, and multiple Pt nanoclusters (≈3 nm) are decorated on SnO$_2$ surface with the lattice distance of 0.227 nm attributing to the (111) planes of Pt. Energy dispersive X-ray spectroscopy (EDS) mappings (Figure S1, Supporting Information) were also conducted to demonstrate the uniform distribution of O, Sn, and Pt elements, confirming the successful Pt/SnO$_2$ sensors design on the AAO substrate.

X-ray diffraction (XRD) and X-ray photoelectron spectroscopy (XPS) spectra were also performed to seek deep insights into the Pt/SnO$_2$ structure. As shown in Figure 3f, the XRD peaks of the SnO$_2$ (green) and Pt/SnO$_2$ (red) samples are well indexed

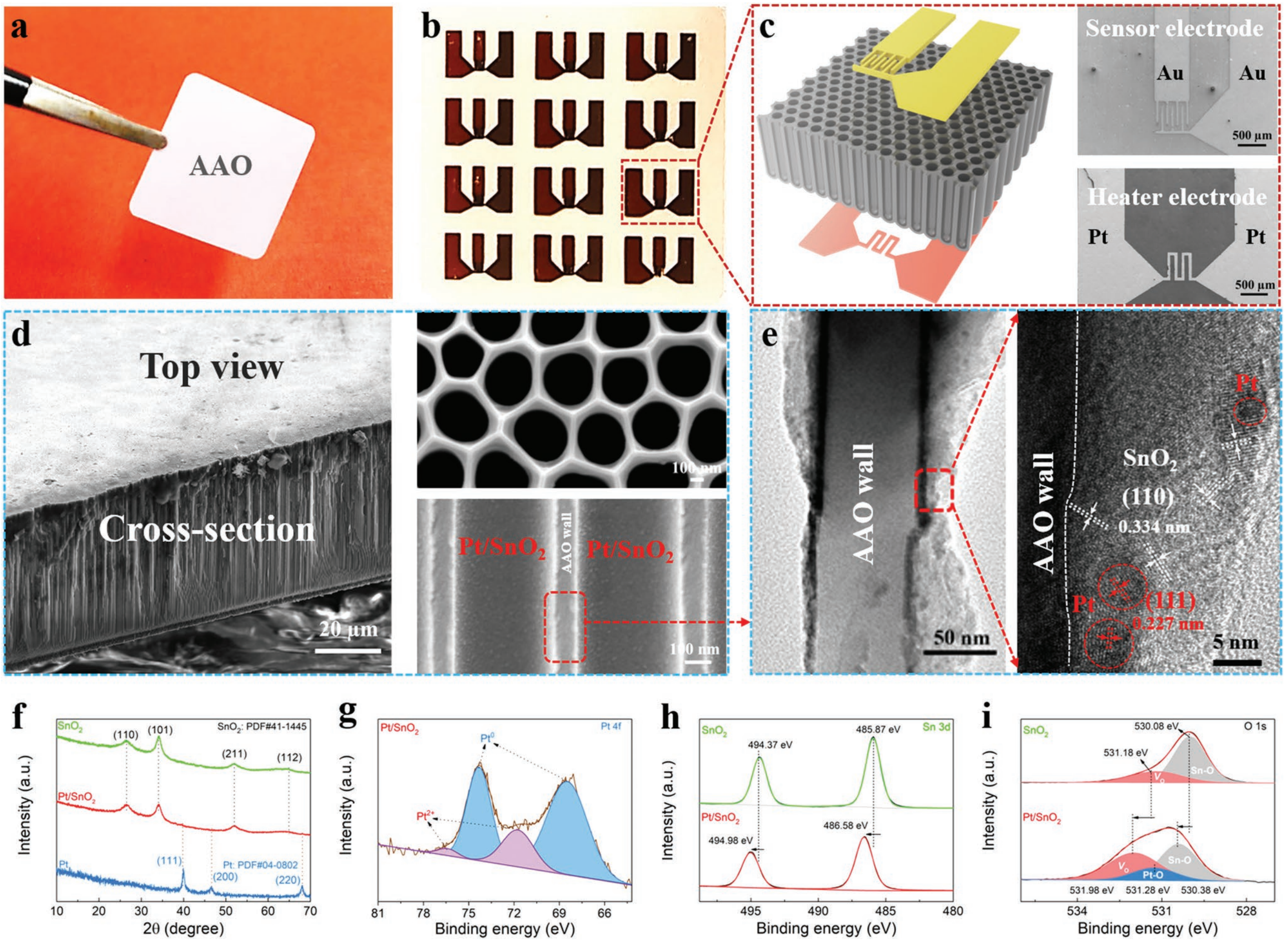

Figure 3. Pt/SnO$_2$ sensor structure. a) Photograph of 2 cm × 2 cm 3D AAO supported Pt decorated SnO$_2$ nanotube array. b) 3 × 4 sensors on 3D AAO substrate. c) The structure diagram of the sensor with three components (sensor electrode, sensing material, and heater electrode). d) The SEM image of the sensing material on AAO substrate (top view and cross-section). e) The HRTEM of the Pt/SnO$_2$ on AAO substrate. f) XRD spectra of Pt, SnO$_2$, and Pt/SnO$_2$. XPS spectra: g) Pt 4f; h) Sn 3d; and i) O 1s.

to the tetragonal rutile structure of SnO$_2$ (JCPDS#41–1445).[44] Blue line shows the XRD spectra of the Pt thin film (60 cycles ALD), which assigns to the face centered cubic (fcc) structure of Pt (JCPDS#04–0802). However, only three cycles of Pt decoration were conducted onto the SnO$_2$ thin film, thus, the Pt nanoclusters have weak peaks that cannot be clearly resolved in XRD analysis due to the low loading below the detection limit. However, XPS spectra are applicable to detect the trace content element and determine the existence of Pt elements in the Pt/SnO$_2$ samples (Figure 3g). The valence state of Pt^{2+} appeared in the Pt/SnO$_2$ sample which was attributed to the partial oxidation happened on the Pt surface. Figure 3h shows the Sn 3d XPS spectra of Pt/SnO$_2$ shifted to higher binding energy compared with that of SnO$_2$, confirming that Pt decoration induced an electron transfer occurring from SnO$_2$ to Pt according to the shielding effect of the outer electrons.[45] In addition, the result can also determine a Schottky junction formation at interferes between Pt and SnO$_2$ due to work function difference of Pt (5.64 eV) and SnO$_2$ (4.4 eV).[46] The surface state of the sensing materials (e.g., adsorbed oxygen species) takes a critical role in the sensing performance. As shown in Figure 3i, O 1s in SnO$_2$ can be split into two peaks, the peak at 530.08 eV could be attributed to the lattice oxygen and the other one at 531.18 eV belongs to the adsorbed oxygen species occupying 19.7%. In the Pt/SnO$_2$ sample, the O 1s binding energies shifts to the higher state (530.38 and 531.98 eV) which is consistent with Sn 3d shifting result. Importantly, the Pt decoration could enhance the ratio of adsorbed oxygen species to 34.2% owing to the catalytic spillover effect, which is beneficial for the gas-sensing improvement.[13,47] The peak at 531.28 eV could be attributed to the Pt–O bond formation at the Pt surface matching the Pd 4f XPS results, and this oxygen species can also contribute to the gas-sensing performance enhancement.

2.4. Pt/SnO$_2$ Sensors for Sensitive and Selective NO$_2$ Sensing

The as-fabricated Pt/SnO$_2$ sensors are used to assess the gas-sensing performance for sensitive and selective NO$_2$ detection. Since the sensors have the integrated micro-heater, the operation temperature can be controlled by the input heating power (Figure S2a, Supporting Information). As shown in **Figure 4**a,

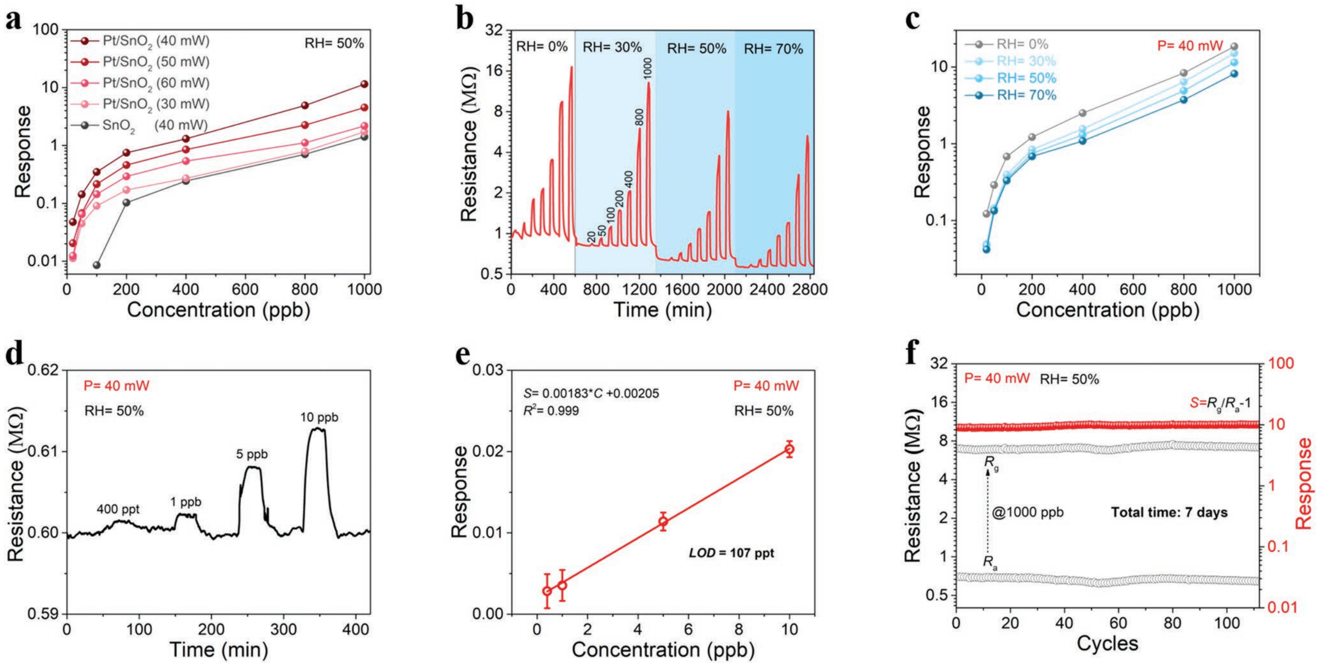

Figure 4. Pt/SnO_2 sensors for sensitive NO_2 sensing. a) NO_2 sensing based on the Pt/SnO_2 sensors operated at different heating power, b,c) NO_2 sensing curves and sensing responses at the optimized operation heating power (40 mW, ≈200 °C) at different RH, d,e) Low-concentration NO_2 detection and the theoretical LOD calculation, f) The long-term stability for NO_2 sensing at the operation condition (40 mW, RH = 50%; one cycle = 1.5 h).

NO_2 sensing performances at different heating powers are examined, and the Pt/SnO_2 sensors achieve the best sensing response at the heating power of 40 mW (≈200 °C), which is superior to that of the pure SnO_2 ones at their optimized heating power (Figure S2b, Supporting Information). The typical real-time sensing curves of the sensors toward NO_2 from 20 to 1000 ppb at the relative humidity (RH) of 0%, 30%, 50% and 70% are shown in Figure 4b. The sensing response (defined as $S = R_g/R_a - 1$, where R_a is the resistance in the presence of clean air and R_g is the resistance in the presence of the target gas) increases with increasing NO_2 concentrations with a marginal baseline resistance drift, and the sensing responses are extracted from the sensing curves and plotted in Figure 4c. The Pt/SnO_2 sensors display a sensing response decay with the increasing RH, while showing negligible sensing response variation at the RH changing from 30% to 70% at such optimized operation temperature, which is highly attractive in practical gas-sensing applications. Moreover, the Pt/SnO_2 sensors demonstrate the capability for the low concentration NO_2 detection as low as 400 ppt (Figure 4d). The theoretical LOD is defined as three times the relative standard deviation (RSD) (σ) of sensor noise divided by the slope of the linear fit[48] (LOD (ppb) = $3 \times \sigma$/slope), and the detailed calculation process was described in the Supporting Information. As a result, *LOD* is calculated to be 107 ppt as shown in Figure 4e, which is the record for metal-oxide gas sensors, to our best knowledge. Most noteworthy is that the Pt/SnO_2 sensors also enable the room-temperature NO_2 sensing down to 2 ppb with LOD of 496 ppt (Figure S3, Supporting Information), superior to most of the reported chemiresistive NO_2 sensors (Table S1, Supporting Information) and well satisfies the LOD requirements by US EPA (53 ppb). In addition, long-term stability is an important characteristic of gas sensors in real-time application, and Figure 4f shows that the Pt/SnO_2 sensors have a relative stable baseline (R_a) and sensing response ($S = R_g/R_a - 1$) at 7 days continuous cycling test (112 cycles in total, each cycle with 0.5 h NO_2 for response and 1 h fresh air flowing for recovery showing in Figure S3c, Supporting Information). Furthermore, the long-term stability of the sensor for NO_2 sensing was conducted for a month (Figure S3d, Supporting Information), which exhibited a marginal response variation. We should also mention that the low-temperature ALD deposition technology can achieve uniform and conformal thin film with a precise thickness control, enabling to realize high device yield and desirable devices repeatability for the large-scale production. As seen in Table S2, Supporting Information, the statistics of the baselines resistance (R_a) and NO_2 sensing response (*S*@1000 ppb) of the 12 devices on a chip (Figure 3b) show minor variation with the RSD to be 8.47% and 8.82%, respectively.

It is well known that NO_2 always exists under the presence of other interfering gases, such as FA, toluene, acetone, and SO_2. Thus, the selective detection of NO_2 among the interfering gases is critical to eliminate the false alarms issues. **Figure 5**a–d shows the Radar map of gas sensing responses toward NO_2 and the interfering gases of SO_2, FA, toluene, and acetone (1000 ppb) at different heating powers from 30 to 60 mW, respectively. The Pt/SnO_2 sensor has the higher sensing response toward the target gas of NO_2, which is also superior to that of the Pd/SnO_2 and Au/SnO_2 sensors for NO_2 sensing (Figure S4a,b, Supporting Information) as estimated by the DFT results. The selectivity of the Pt/SnO_2 sensor to NO_2 over interfering gases (S_{NO_2}/S_X, X = SO_2, FA, toluene, or acetone) were calculated (Figure S4c, Supporting Information). Note that the ratio $S_{NO_2}/S_X > 1$ indicates the selective detection of NO_2 over the

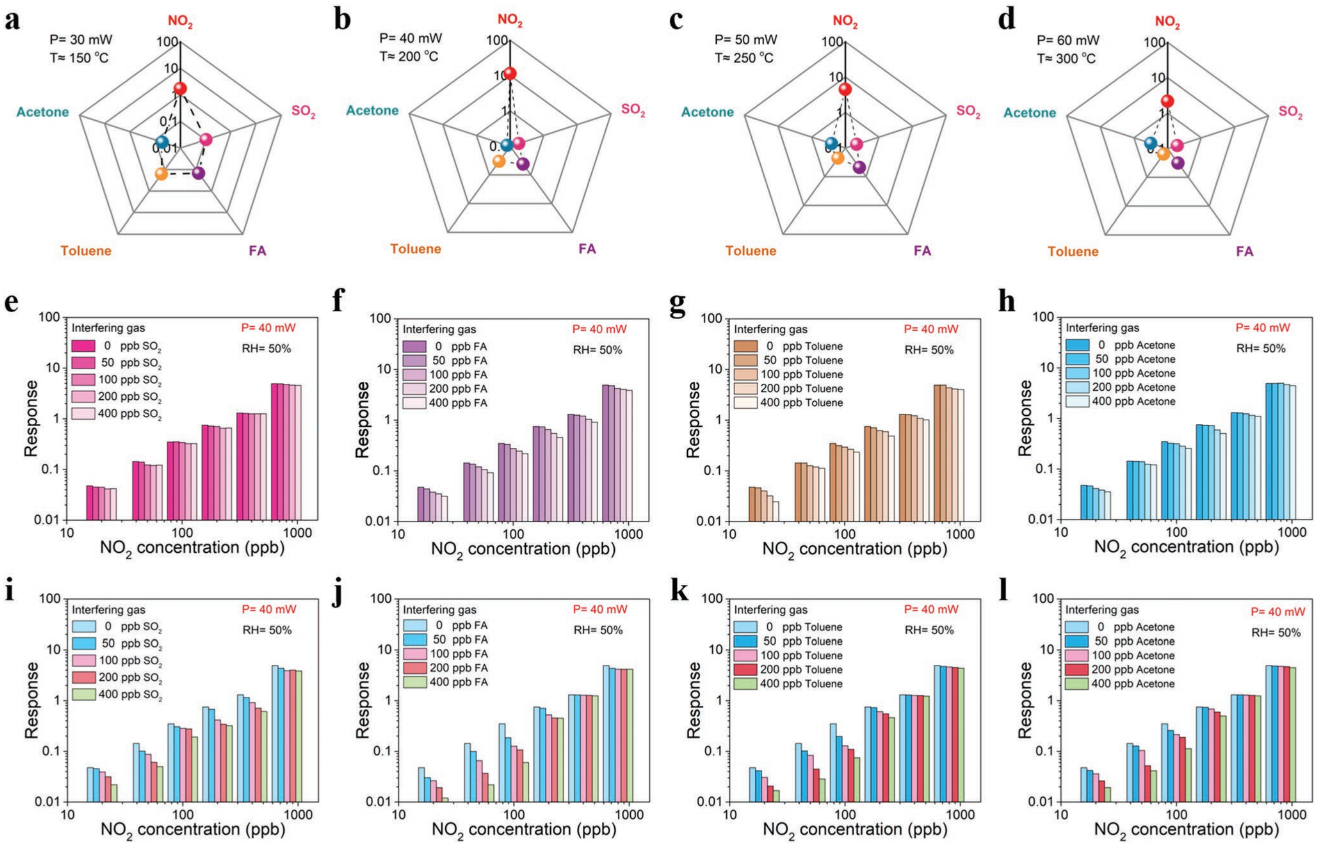

Figure 5. Pt/SnO_2 sensors for selective NO_2 sensing. The Radar map of gases response (1000 ppb) at different heating power: a) 30 mW (≈150 °C); b) 40 mW (≈200 °C); c) 50 mW (≈250 °C); d) 60 mW (≈300 °C); NO_2 sensing from 20 to 1000 ppb at the stable baseline of the interfering gases e) SO_2, f) FA, g) toluene, and h) acetone, mixture with air (RH = 50%); NO_2 sensing from 20 to 1000 ppb mixture with the interfering gases of i) SO_2, j) FA, k) toluene, and l) acetone, respectively, at the stable baseline of air (RH = 50%).

interfering gases; the larger ratio, the better selectivity.[49] The Pt/SnO_2 sensor achieves the optimal selectivity for NO_2 sensing at the heating power of 40 mW, and the response ratios can reach to 62.9 (S_{NO_2}/S_{SO_2}), 27.2 (S_{NO_2}/S_{FA}), 34.1 ($S_{NO_2}/S_{toluene}$), and 92.8 ($S_{NO_2}/S_{acetone}$), respectively.

Considering the real environment of the gases in the mixture state, we use two scenarios to further evaluate the sensor selectivity that have been rarely investigated previously. In the first scenario, we assume the interfering gases already exist in the environment leading to a stable resistance baseline of the sensor. Then the target gas is admitted in, resulting in a sensing response ($\overline{S}_{NO_2}$). Comparing the sensing response with ($\overline{S}_{NO_2}$) and without (S_{NO_2}) the existence of the interfering gas, we can evaluate the sensor selectivity in gas mixtures. The sensing curves for NO_2 (20 to 1000 ppb) sensing in the existence of the interfering gases of SO_2, FA, toluene, and acetone were shown in Figure S5a–d, Supporting Information, respectively. The sensing responses ($\overline{S}_{NO_2}$) were calculated from the sensing curves and plotted in Figure 5e–h, respectively. We observed that the NO_2 sensing responses had a small degradation in the existence of the interfering gas with the concentration from 0 to 400 ppb, proving the capability of the sensor for the selective NO_2 sensing in the gas mixtures. The other scenario is to test the sensing response ($\overline{\overline{S}}_{NO_2}$) of the mutual mixture of the target gas of NO_2 and another interfering gas. The sensing curves for NO_2 (20 to 1000 ppb) sensing in the mutual mixture of SO_2, FA, toluene, and acetone are displayed in Figure S5e–h, Supporting Information, respectively. The sensing responses ($\overline{\overline{S}}_{NO_2}$) are calculated from the sensing curves and plotted in Figure 5i–l, respectively. It shows that in such a mixture state, the interfering gases had a larger influence on the sensing response especially for the low concentration NO_2 sensing. Fortunately, the Pt/SnO_2 sensor still possesses the capability for selective NO_2 sensing even with the interfering gas at the concentration of 400 ppb.

2.5. The Mechanism for Sensitive and Selective NO_2 Sensing

The electrical and chemical interaction between the sensing material and the target gas depends on the available free energy of gas-sensing materials that can provide appropriate adsorption energy (E_{ads}) and activation energy (E_a) favorable for a specific reaction.[50,51] The possible reaction is as follows:

$$O_2 + e^- \rightarrow O^{n-}(O_2^-, O^-, \text{ or } O^{2-}) \tag{5}$$

$$NO_2 + e^- \rightarrow NO_2^- \tag{6}$$

$$NO_2 + O^{n-} + e^- \rightarrow NO_3^- \tag{7}$$

First, the atmospheric oxygen is chemisorbed on the surface forming O_2^-, O^-, or O^{2-} by capturing the electrons from sensing materials, and when exposed to the target gas NO_2, the molecules not only directly obtained electrons from the surface of the sensing materials to form NO_2^-, but also reacted with the chemisorbed oxygen and were converted into NO_3^-. In addition, the formation of the Schottky junction at the Pt–SnO_2 interface, as well as the catalytic effect of Pt, would strengthen the chemical and electronic interaction for the gas-sensing improvement.[13] DFT calculations are carried out to further investigate the interaction between the sensing materials and the gases. The adsorption configurations and differential charge density are shown in **Figure 6**a–c and the calculated E_{ads} and Bader charge (Δq) are summarized in Figure 6d. The negative E_{ads}

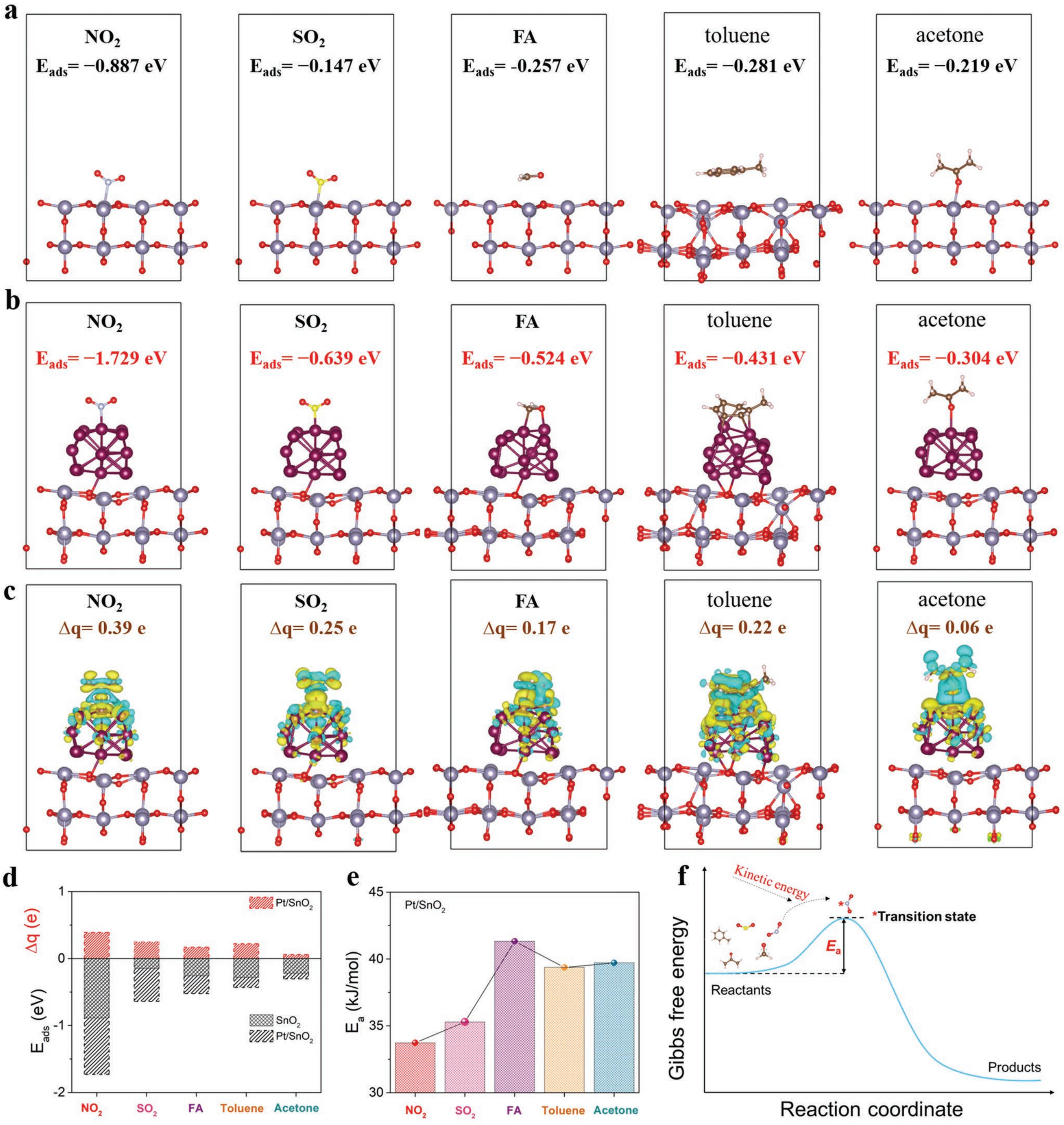

Figure 6. The proposed mechanism for sensitive and selective NO_2 sensing. Calculated adsorption energy toward the gases of NO_2, SO_2, FA, toluene, and acetone on a) SnO_2, and b) Pt/SnO_2, respectively. c) Differential charge density of NO_2, SO_2, FA, toluene, and acetone adsorbed on Pt/SnO_2 (yellow represents charge accumulation and cyan represents charge lose). d) Gas adsorption energy comparison on SnO_2 and Pt/SnO_2; e) Calculated activation energy of Pt/SnO_2 toward NO_2, SO_2, FA, toluene, and acetone. f) Possible surface reaction on Pt/SnO_2 relating to the activation energy.

indicates that all the adsorptions are thermodynamically preferable on the sensing materials, and Pt/SnO_2 shows the stronger adsorption capability toward the gases NO_2, SO_2, FA, toluene, and acetone than that of the SnO_2. Specifically, Pt/SnO_2 possesses the highest E_{ads} toward the target gas of NO_2. And the calculated differential charge density results also show Pt/SnO_2 has the larger Bader charge of 0.39 e than that of SO_2 (0.25 e), FA (0.17 e), toluene (0.22 e), and acetone (0.06 e), respectively. All the results imply a strong chemisorption of the NO_2 molecules on the Pt/SnO_2 surface, consistent with sensitive and selective NO_2 sensing results. Meanwhile, the activation energies (E_a, the minimum energy needed for a surface chemical reaction to occur) have been calculated according to Arrhenius equation (Figure S6, Supporting Information), and the calculated E_a were shown in Figure 6e. The Pt/SnO_2 exhibited an E_a of 33.73 kJ mol^{-1} toward NO_2, lower than the interfering gases of SO_2 (35.29 kJ mol^{-1}), FA (41.32 kJ mol^{-1}), toluene (39.37 kJ mol^{-1}), and acetone (39.71 kJ mol^{-1}), suggesting a favorable surface interaction between the Pt/SnO_2 and NO_2. Ultimately, the proposed mechanism for sensitive and selective NO_2 sensing is described in Figure 6f. The surface of Pt/SnO_2 provides strongest E_{ads} and lowest E_a toward NO_2, and NO_2 molecules will obtain the kinetics energy from the lattice vibration under operation temperature, preferentially overcoming the activation barrier for the surface reaction, resulting in the selective NO_2 detection. However, the further increased operation temperature will provide enough energy for all the other gases overcoming their activation barrier, deteriorating the selectivity. Thus, the rational design of the sensors assisted with the operation temperature modulation, enables the sensitive and selective NO_2 detection among the interfering gases.

2.6. Real-Time Indoor and On-Road NO_2 Detection

To demonstrate the potential applications of the sensor for selective indoor and on-road NO_2 detection, a portable wireless NO_2 sensor system on the printed circuit board (PCB) is designed, and the detailed circuit designs are shown in Figure S7, Supporting Information. The sensor box (**Figure 7**a) consists of a power supply module (lithium battery, 800 mAh), sensor module, microcontroller-analog readout circuit, and wireless data transmission module (MCU&Bluetooth low energy [BLE] unit, ESP32MINI1). The BLE unit enables the wireless connection between the sensor module and the mobile phones, displaying the NO_2 concentration and safety level (Figure 7b). For the practical application, we use the static testing method instead of the dynamic testing to simulate real environment for the sensor devices calibration. We placed the sensor device in the testing chamber (40 cm × 40 cm × 30 cm = 48 L) and injected a certain concentration of target NO_2, and the input gas concentrations of NO_2 were calibrated by the Thermo Scientific 42iQ Trace Level NO–NO_2–NO_X Analyzer. The sensor had a fast response/ recovery time within 30 and 150 s, respectively (Figure S8a, Supporting Information). After this calibration, we can obtain the relationship between the response ($S = R_a/R_g–1$) and the concentration (*Con.*) (Figure S8b, Supporting Information). And then, the obtained equation (*Con.* = 403 × *S*^0.38) was written into the program of the mobile App, as long as our sensor has response to NO_2, we can obtain the exact output NO_2 gas concentration. Next, the sensor system is utilized for the real-time indoor and on-road NO_2 detection (Figure 7c,d). The sensing signals are recorded and transmitted to a smartphone in real time via a wireless Bluetooth protocol, showing the dynamic response and recovery NO_2 sensing, which can be clearly seen from the Videos S1–S3, Supporting Information. All these results suggest that the as-designed sensors can effectively carry out the tasks for in indoor/outdoor environmental monitoring, especially for NO_2 selective detection.

3. Conclusions

We demonstrate a unique sensor design using Pt nanoclusters decorated 3D metal oxide (SnO_2) nanotube array for the sensitive and selective NO_2 sensing. The sensor achieves an ultrahigh sensitivity to NO_2 with the record LOD down to 107 ppt assisted with an operation temperature modulation, and it also enables the selective NO_2 sensing suppressing the responses to interfering gases (e.g., SO_2, FA, acetone, and toluene). Furthermore, a portable wireless NO_2 sensor system has been developed. It can communicate with smart phone displaying the NO_2 concentration and safety level in real-time indoor/outdoor environmental monitoring applications. Overall, our rational sensor design and the successful demonstration clearly show the enticing potential of our nanostructure gas sensors for future environmental safety and air quality monitoring in smart homes and smart cities.

4. Experimental Section

Sensor Film Deposition: The sensor was fabricated by a two-step ALD method.[13] SnO_2 was first deposited on the 3D AAO substrate at 150 °C, the Sn precursor of $Sn(DMA)_4$ in a bubbler (70 °C) and H_2O were successively introduced into the chamber using high purity N_2 (99.9999%) as the carrier and purge gas. The SnO_2 ALD pulse sequence (1 cycle) consisted of $Sn(DMA)_4$ injection (700 ms)/purge (30 s)/wait (5 s), followed by H_2O (70 ms)/purge (30 s)/wait (5 s), and the thickness was controlled by the ALD recipe for 45 cycles and then annealed at 450 °C for 12 h. For the overlayer of Pt decoration, the pulse sequence (1 cycle) consisted of $MeCpPtMe_3$ injection (1000 ms)/purge (30 s)/wait (5 s), followed by N_2H_4 (200 ms)/purge (30 s)/wait (5 s), and the thickness was controlled by the ALD recipe for 3 cycles.

Sensor Fabrication: The sensor on one-chip AAO was covered by a shadow mask and sputtered top patterned Au electrodes (180 nm) and bottom Pt heater electrodes (180 nm).

Characterization: Scanning electron microscope (SEM, JSM-7100F, JEOL) and high-resolution transmission electron microscope (HR-TEM, JEM 2010F, JEOL) were performed to characterize the morphology and size of the thin films. A VG Multilab 2000 system with an Al Kα source to carry out the XPS measurements with the C 1s peak at 284.6 eV as the reference, was used. XRD measurements (MAXima_X XRD-7000, Shimadzu, Japan) were performed with Cu Kα radiation in the 2θ range of 10–70°.

Gas-Sensing Measurement: The controlled amount of NO_2, SO_2, FA, toluene, and acetone were introduced using mass flow controllers (MFC1-5), respectively, and each gas was intermixed with air injected from MFC6 to control the gas concentration. The total flow rate was controlled at 500 sccm. The gas was introduced into the chamber (8 cm × 8 cm × 4 cm) and the sensor resistance was recorded as a function of time at the fixed voltage of 3.3 V.

Figure 7. Real-time indoor and on-road NO_2 detection. a,b) Wireless NO_2 sensor system that can communicate with smartphone. Potential applications for c) indoor and d) on-road NO_2 monitoring.

Supporting Information

Supporting Information is available from the Wiley Online Library or from the author.

Acknowledgements

This work was supported by the Science and Technology Plan of Shenzhen (JCYJ20180306174923335 and JCYJ20170818114107730), the General Research Fund (Nos. 16205321 and 16214619) from the Hong Kong Research Grant Council, Innovation Technology Fund (GHP/014/19SZ), the Guangdong-Hong Kong-Macao Intelligent Micro-Nano Optoelectronic Technology Joint Laboratory (project no. 2020B1212030010), the Foshan Innovative and Entrepreneurial Research Team Program (2018IT100031), the Zhongshan Municipal Science and Technology Bureau (ZSST21EG05), and Z.L.S. thanks the support of the National Natural Science Foundation of China (No. 62004084). The authors acknowledge support received from the Material Characterization and Preparation Facility (MCPF), the Nanosystem Fabrication Facility (NFF), the Center for 1D/2D Quantum Materials and the State Key Laboratory on Advanced Displays and Optoelectronics at HKUST, and the MNT Micro and Nanotech Co., LTD at Wuxi, Jiangsu, China.

Conflict of Interest

The authors declare no conflict of interest.

Data Availability Statement

The data that support the findings of this study are available from the corresponding author upon reasonable request.

Keywords

3D metal oxide gas sensors, parts per trillion, Pt nanoclusters, selective NO_2 sensing, wireless sensor systems

Received: July 2, 2022
Revised: July 28, 2022

[1] K. Lim, Y. M. Jo, J. W. Yoon, J. S. Kim, D. J. Lee, Y. K. Moon, J. W. Yoon, J. H. Kim, H. J. Choi, J. H. Lee, *Small* **2021**, *17*, 2100438.
[2] Z. Chen, Z. Chen, Z. Song, W. Ye, Z. Fan, *J. Semicond.* **2019**, *40*, 111601.
[3] H. J. Han, G. R. Lee, Y. Han, H. Jang, E. N. Cho, S. Kim, C. S. Kim, S. Yim, J. W. Jeong, J. M. Kim, S. Yu, H. L. Tuller, Y. S. Jung, *Adv. Funct. Mater.* **2021**, *32*, 2108891.
[4] Z. Ren, D. Qi, P. Sonar, Z. Wei, *J. Semicond.* **2020**, *41*, 040402.
[5] Y. J. Su, J. J. Wang, B. Wang, T. N. Yang, B. X. Yang, G. Z. Xie, Y. H. Zhou, S. L. Zhang, H. L. Tai, Z. X. Cai, G. R. Chen, Y. D. Jiang, L. Q. Chen, J. Chen, *ACS Nano* **2020**, *14*, 6067.
[6] X. Pan, X. Zhao, A. Bermak, Z. Fan, *IEEE Electron Device Lett.* **2016**, *37*, 92.
[7] M. Mele, C. Magazzino, N. Schneider, V. Strezov, *Environ. Res.* **2021**, *194*, 110663.
[8] L. Zhang, Z. Li, J. Liu, Z. Peng, J. Zhou, H. Zhang, Y. Li, *Anal. Chem.* **2020**, *92*, 11277.
[9] G. S. Kim, Y. Park, J. Shin, Y. G. Song, C. Y. Kang, *Sensors* **2021**, *21*, 1922.
[10] K. Toda, T. Koga, J. Kosuge, M. Kashiwagi, H. Oguchi, T. Arimoto, *Anal. Chem.* **2009**, *81*, 7031.
[11] Y. Su, J. Wang, B. Wang, T. Yang, B. Yang, G. Xie, Y. Zhou, S. Zhang, H. Tai, Z. Cai, G. Chen, Y. Jiang, L. Chen, J. Chen, *ACS Nano* **2020**, *14*, 6067.
[12] Z. Song, Z. Hu, J. Liu, J. Yan, H. Li, J. Jiang, J. Tang, H. Liu, *Adv. Electron. Mater.* **2021**, *8*, 2101049.
[13] Z. Song, W. Ye, Z. Chen, Z. Chen, M. Li, W. Tang, C. Wang, Z. Wan, S. Poddar, X. Wen, X. Pan, Y. Lin, Q. Zhou, Z. Fan, *ACS Nano* **2021**, *15*, 7659.
[14] W. Tang, Z. Chen, Z. Song, C. Wang, Z. Wan, J. Chan, Z. Chen, W. Ye, Z. Fan, *ACS Nano* **2022**, *16*, 10968.
[15] Z. Fan, J. G. Lu, *Appl. Phys. Lett.* **2005**, *86*, 123510.
[16] Z. Fan, D. Wang, P. Chang, W. Tseng, J. Lu, *Appl. Phys. Lett.* **2004**, *85*, 5923.
[17] Y. Su, G. Xie, H. Tai, S. Li, B. Yang, S. Wang, Q. Zhang, H. Du, H. Zhang, X. Du, Y. Jiang, *Nano Energy* **2018**, *47*, 316.
[18] Y. Su, M. Yao, G. Xie, H. Pan, H. Yuan, M. Yang, H. Tai, X. Du, Y. Jiang, *Appl. Phys. Lett.* **2019**, *115*, 073504.
[19] Q. Yuan, Z. Ma, S. Li, L. Pan, *J. Semicond.* **2019**, *40*, 030401.
[20] Y. He, X. Wang, Y. Gao, Y. Hou, Q. Wan, *J. Semicond.* **2018**, *39*, 011005.
[21] Y. Su, G. Chen, C. Chen, Q. Gong, G. Xie, M. Yao, H. Tai, Y. Jiang, J. Chen, *Adv. Mater.* **2021**, *33*, 2101262.
[22] Y. Su, W. Li, L. Yuan, C. Chen, H. Pan, G. Xie, G. Conta, S. Ferrier, X. Zhao, G. Chen, H. Tai, Y. Jiang, J. Chen, *Nano Energy* **2021**, *89*, 106321.
[23] B. Liu, A. Libanori, Y. Zhou, X. Xiao, G. Xie, X. Zhao, Y. Su, S. Wang, Z. Yuan, Z. Duan, J. Liang, Y. Jiang, H. Tai, J. Chen, *ACS Appl. Mater. Interfaces* **2022**, *14*, 7301.
[24] Y. Jian, W. Hu, Z. Zhao, P. Cheng, H. Haick, M. Yao, W. Wu, *Nano-Micro Lett.* **2020**, *12*, 71.
[25] E. P. Olle, J. Farre-Llados, J. Casals-Terre, *Sensors* **2020**, *20*, 5478.
[26] N. Yamazoe, *Sens. Actuators, B* **1991**, *5*, 7.
[27] D. Degler, U. Weimar, N. Barsan, *ACS Sens.* **2019**, *4*, 2228.
[28] D. Han, L. Zhai, F. Gu, Z. Wang, *Sens. Actuators, B* **2018**, *262*, 655.
[29] S. Abegg, D. K. Cerrejon, A. T. Güntner, S. E. Pratsinis, *Nanomaterials* **2020**, *10*, 1170.
[30] J. Chen, Z. Chen, F. Boussaid, D. Zhang, X. Pan, H. Zhao, A. Bermak, C. Tsui, X. Wang, Z. Fan, *ACS Nano* **2018**, *12*, 6079.
[31] X. Pan, X. Liu, A. Bermark, Z. Fan, *ACS Nano* **2013**, *7*, 9318.
[32] X. Pan, X. Zhao, J. Chen, A. Bermak, Z. Fan, *Sens. Actuators, B* **2014**, *206*, 764.
[33] K. Kim, P. G. Choi, T. Itoh, Y. Masuda, *ACS Appl. Mater. Interfaces* **2020**, *12*, 51637.
[34] G. Muller, J. D. Prades, A. Hackner, A. Ponzoni, E. Comini, G. Sberveglieri, *Nanomaterials* **2018**, *8*, 1017.
[35] N. K. Chowdhury, B. Bhowmik, *Nanoscale Adv.* **2021**, *3*, 73.
[36] M. Weber, O. Graniel, S. Balme, P. Miele, M. Bechelany, *Nanomaterials* **2019**, *9*, 1552.
[37] Y. K. Moon, S.-Y. Jeong, Y. C. Kang, J.-H. Lee, *ACS Appl. Mater. Interfaces* **2019**, *11*, 32169.
[38] J. van den Broek, A. T. Guntner, S. E. Pratsinis, *ACS Sens.* **2018**, *3*, 677.
[39] S. Abegg, L. Magro, J. van den Broek, S. E. Pratsinis, A. T. Güntner, *Nat. Food* **2020**, *1*, 351.
[40] S.-Y. Jeong, J.-W. Yoon, T.-H. Kim, H.-M. Jeong, C.-S. Lee, Y. C. Kang, J.-H. Lee, *J. Mater. Chem. A* **2017**, *5*, 1446.
[41] I. C. Weber, H. P. Braun, F. Krumeich, A. T. Guntner, S. E. Pratsinis, *Adv. Sci.* **2020**, *7*, 2001503.
[42] J. Wang, S. Fan, Y. Xia, C. Yang, S. Komarneni, *J. Hazard. Mater.* **2020**, *381*, 120919.
[43] H. Zhang, Y. Wang, X. Zhu, Y. Li, W. Cai, *Sens. Actuators, B* **2019**, *280*, 192.
[44] Z. Song, J. Yan, J. Lian, W. Pu, L. Jing, H. Xu, H. Li, *ACS Appl. Nano Mater.* **2020**, *3*, 6385.
[45] J. Yan, Z. Song, H. Li, H. Xu, L. Y. S. Lee, *Chem. Eng. J.* **2021**, *425*, 131512.
[46] C. Körber, S. P. Harvey, T. O. Mason, A. Klein, *Surf. Sci.* **2008**, *602*, 3246.
[47] M. Lei, M. Gao, X. Yang, Y. Zou, A. Alghamdi, Y. Ren, Y. Deng, *ACS Appl. Mater. Interfaces* **2021**, *13*, 51933.
[48] Z. Song, Z. Wei, B. Wang, Z. Luo, S. M. Xu, W. K. Zhang, H. X. Yu, M. Li, Z. Huang, J. Zang, F. Yi, H. Liu, *Chem. Mater.* **2016**, *28*, 1205.
[49] H. S. Woo, C. W. Na, J. H. Lee, *Sensors* **2016**, *16*, 1531.
[50] Q. Rong, B. Xiao, J. Zeng, R. Yu, B. Zi, G. Zhang, Z. Zhu, J. Zhang, J. Wu, Q. Liu, *ACS Sens.* **2022**, *7*, 199.
[51] M. Zhu, P. Tian, M. E. Ford, J. Chen, J. Xu, Y.-F. Han, I. E. Wachs, *ACS Catal.* **2020**, *10*, 7857.